Interaction of spin-orbital-lattice degrees of freedom: Vibronic state of the corner-sharing-tetrahedral frustrated spin system HoBaFe$_4$O$_7$ by dynamical Jahn-Teller effect

Kazuya Kamazawa,[1] Motoyuki Ishikado,[1] Seiko Ohira-Kawamura,[2] Yukinobu Kawakita,[2]
Kazuhisa Kakurai,[1] Kenji Nakajima,[2] and Masatoshi Sato[2]

[1]*Comprehensive Research Organization for Science and Society (CROSS), Tokai, Ibaraki 319-1106, Japan*
[2]*J-PARC Center, Japan Atomic Energy Agency (JAEA), 2-4, Shirakata, Tokai, Ibaraki 319-1195, Japan*

A powder inelastic neutron-scattering study of HoBaFe$_4$O$_7$ (HBFO) revealed characteristic magnetic excitations associated with geometrical spin frustration. Dispersionless excitations in energy (ω) and wave-vector (Q) space are observed at several discrete energies. Some of them can be attributed to crystal-field excitations of Ho^{3+} in octahedral symmetry, but the others are explained instead by the vibronic state of the Fe^{2+} dynamical Jahn-Teller effect with orbit-spin coupling, indicating interaction among the spin, the orbital, and the lattice degree of freedom. The antiferromagnetic HBFO lattice has cubic symmetry, and both Fe^{2+} and Fe^{3+} reside on corner-sharing tetrahedra with a number ratio of 3:1. Even though Fe^{2+} is a Jahn-Teller active ion in tetrahedral symmetry, the system does not exhibit any static lattice distortion to the lowest temperature studied (4 K). The observed excitations can be understood by considering the dynamical interaction among spin-orbital-lattice degrees of freedom, indicating that spin fluctuation due to the frustration effect induces the dynamical Jahn-Teller effect, although in most cases a Jahn-Teller active ion Fe^{2+} takes the static Jahn-Teller effect in a magnetic oxide system.

I. INTRODUCTION

Frustrated spin systems exhibit a variety of physical phenomena, such as strong suppression of magnetic ordering temperature T_N and nontrivial magnetic order. Up to now, the study of frustrated spin systems has been focused mainly on the ground state and/or a relatively small energy ($\omega \sim 0$) region [1–3]. In neutron scattering studies, characteristic scattering patterns have been reported for C15 Laves [4], spinel [5,6], pyrochlore [7–9], garnet [10], etc. [11]. However, recent work using neutron-scattering measurements has shifted to investigating spin dynamics in wide energy (ω) and wave-vector (Q) regions. Thanks to recent developments in neutron-scattering technology, in particular facilities with chopper-type spectrometers, we can easily access wide ω and Q regions at once with high-intensity and low-background signals. Accordingly, a lot of neutron time-of-flight work on frustrated systems has been carried out [12–15]. Regardless of quantum and classical system, spin dynamics are considered an even more critical issue in frustrated spin systems.

To extract pure frustration effects of spin dynamics, a three-dimensional classical spin system is ideal because spin fluctuation is not disturbed by either the quantum effect or the low-dimensional effect [16] as an origin of fluctuation of physical properties. Therefore, we carried out a neutron-scattering measurement for YBaFe$_4$O$_{7-\delta}$ (YBFO) [17] recently, and we found streaklike magnetic scattering extending up to at least $\omega \sim 80$ meV [18], around $Q = Q_p$ ($\sim$1.25 Å^{-1}), which corresponds to the hexagon correlation of Fe spins. Although at first glance streaklike scattering resembles that of itinerant electron systems [4,19,20], it can also be found in oxide systems with a lattice consisting of corner-sharing tetrahedra [17,21]. We interpret streak scattering as instantaneous antiferromagnetic correlation within hexagon spin clusters, that is, spins are fluctuating in a wide energy range maintaining this type of correlation. The observed behavior is attributable to a frustrated spin nature.

In oxide insulators of RBaFe$_4$O$_7$ (RBFO) (R = Y, Lu, In, Sc, Dy, Ho, Yb, etc.), with a relatively small ionic radius of R, the crystal structure tends to have cubic symmetry [23–26]. The number ratio of Fe^{2+} and Fe^{3+} is 3:1, and both ions reside on corner-sharing tetrahedra. Although in most cases a Jahn-Teller active ion Fe^{2+} takes the static Jahn-Teller effect in a magnetic oxide system, the system does not exhibit any static lattice distortion to the lowest temperature, and any charge ordering such as Fe$_3$O$_4$ [27–29] is not reported [24], that is, the system is an insulator in the entire temperature range.

Interestingly, for the R = Ho case, effective magnetic moments of Fe ions are estimated to be quite a bit smaller [22] than those of YBaFe$_4$O$_{7-\delta}$ (YBFO) [17] in a magnetic susceptibility measurement. In the present paper, we report a neutron inelastic-scattering study on HoBaFe$_4$O$_7$ (HBFO), and we present an aspect of the frustrated spin feature. In this way, we can systematically investigate a variety of excitations by R ion substitution, and these investigations provide other opportunities for studying pure frustration effects, because the ligand field of cations at Fe sites is different from that of spinel and pyrochlore.

II. SAMPLE PREPARATION AND EXPERIMENTAL METHOD

A powder sample of HBFO with cubic symmetry (space group $F\bar{4}3m$) was prepared by a two-step solid-state reaction. First, a mixture of BaCO$_3$ and Fe$_2$O$_3$ with a molar ratio of 1 : 1 was ground and pressed into pellets, which were heated at 1200 °C for 12 h in air to obtain BaFe$_2$O$_4$. Next, a stoichiometric mixture of Ho$_2$O$_3$, BaFe$_2$O$_4$, Fe, and Fe$_2$O$_3$ was ground and pressed into pellets, which were heated at 1100 °C for 24 h in argon gas. A magnetic susceptibility measurement
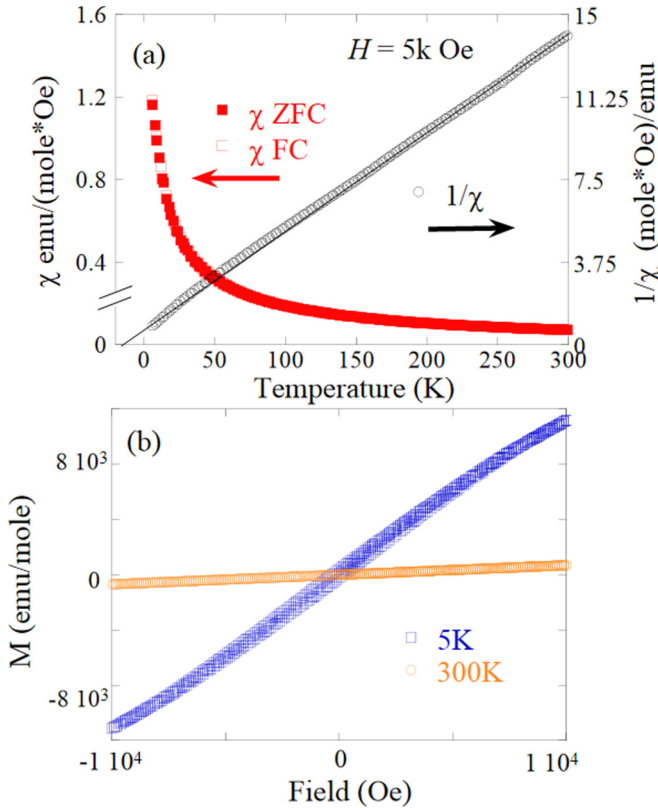
FIG. 1. (a) Magnetic susceptibility (χ) -temperature (T) curves measured under zero-field-cooling [ZFC (closed symbols)] and field-cooling [FC (open symbols)] conditions with the magnetic field $H = 5k$ Oe. The inverse magnetic susceptibility $1/\chi$ is also shown. (b) M-H curves at $T = 5$ and 300 K.

was performed with a SQUID system. We confirmed that no impurities have been found in x-ray diffraction and neutron-scattering measurements. The neutron-scattering measurement was carried out with the spectrometer AMATERAS (BL-14) [30] located at Materials and Life Science Experimental Facility (MLF) of Japan Proton Accelerator Research Complex (J-PARC). We used multi-incident neutron energies with E_i of 27.59, 11.66, and 6.389 meV. The sample was loaded into a sample can made of aluminum. All neutron-scattering data were analyzed with the software suite UTSUSEMI [31].

III. RESULTS AND DISCUSSION

A. Magnetic susceptibility

Figure 1(a) shows the magnetic susceptibility and inverse magnetic susceptibility versus temperature (T) curves of HBFO under a magnetic field (H) of 5k Oe. The field-cooling (FC) and zero-field-cooling (ZFC) curves trace almost the same path over the whole temperature range. Any apparent sign of antiferromagnetic correlation cannot be seen in the curves, but it does not always suggest that correlations of Fe spins are absent. Figure 1(b) shows the M-H curves of HBFO at $T = 5$ and 300 K, indicating HFBO is a paramagnetic at room temperature. From the inverse magnetic susceptibility in Fig. 1(a), the Curie-Weiss temperature Θ is estimated to be -18 K, and the Curie constant is 23.98 emu/K/mol.

Then the effective magnetic moment of HBFO is estimated to be $2.77\mu_B$/magnetic ion. It is significantly smaller than the simple sum of the spin moments of Ho^{3+} and the high spin state of Fe^{2+} and Fe^{3+}, even though there is not the interaction between Ho and Fe ions. Compared to the distance between Fe ions, ~ 3 Å, since the distance between Ho ions is ~ 6 Å and is too far to be effective, the interaction between Fe and Ho sublattices is negligible. We have summarized the discussion as a separated work, and it is given in another report [22].

B. Neutron scattering

The neutron-scattering intensity (I) maps at 4 K in ω-Q space of HBFO are shown in Fig. 2 for various incident energies E_i. In Fig. 3, the data with a Bose factor correction are shown for a fixed E_i of 27 meV at several temperatures. The streaklike scattering at $Q \sim 1.25$ Å^{-1} is not clear in HBFO as compared with the YBFO case [17]. We can see discrete dispersionless excitations at, e.g., 0.8, 2.3, 5–7, 10.5, and 16 meV in Figs. 2 and 3. At low temperatures, the 10.5 and 16 meV excitations are clearly observed, but the 5 meV excitation is rather obscure. With increasing T, the 5–7 meV excitation becomes clearer, but the 10.5 and 16 meV excitations have opposite behavior, suggesting that the 5–7 meV excitation has a phonon origin, and the 10.5 and 16 meV excitations have a magnetic origin. The details will be discussed in Sec. III B 2.

1. Elastic-scattering data

Figure 4(a) shows the elastic-scattering profiles along the Q direction of the $I(Q,\omega)$ maps (Figs. 2 and 3 of $E_i = 27$ meV), which were obtained by integrating over the sliced region of $-1 \leqslant |\omega| \leqslant 1$ meV at $T = 4$ and 200 K. Here, to see the T difference easily, the baseline (background) of each profile is shifted slightly. It is noted that the d-resolution on the elastic profile of sliced $I(Q, \omega)$ observed by chopper spectrometers is coarser than that of diffractometers, because the design concepts of chopper spectrometers and diffractometers are different. Chopper spectrometers are optimized for taking inelastic-scattering (INS) data, while diffractometers focus on taking only elastic-scattering data. Therefore, we have evaluated the structural distortion of HBFO by the minimum instrumental d-resolution $\Delta d/d \sim 2.9\%$ ($E_i = 6$ meV at $Q \sim 3$ Å) from the full width at half-maximum of Bragg reflections in the high-Q position. Although in most cases a Jahn-Teller active ion Fe^{2+} in tetrahedral symmetry causes a few percent order of lattice distortion [32], no peak broadening or splitting was detected in HBFO down to the lowest T we studied. Considering that the HBFO system maintains cubic symmetry, we can ensure octahedral (O_h) coordination without deformation. Only the thermal contraction of bond lengths is obtained, as shown in the inset of Fig. 4(a). Figure 4(b) show the temperature dependences of the elastic profiles taken with $E_i = 27$ (top) and 6 meV (bottom) to emphasize the magnetic diffuse scattering. The scattering intensity gradually increases with decreasing temperature. The peak top position of $Q_p = 1.25$ Å^{-1} is the same as the characteristic wave-vector position of isostructural YBFO, and it suggests that the antiferromagnetic correlation within an Fe hexagon cluster develops
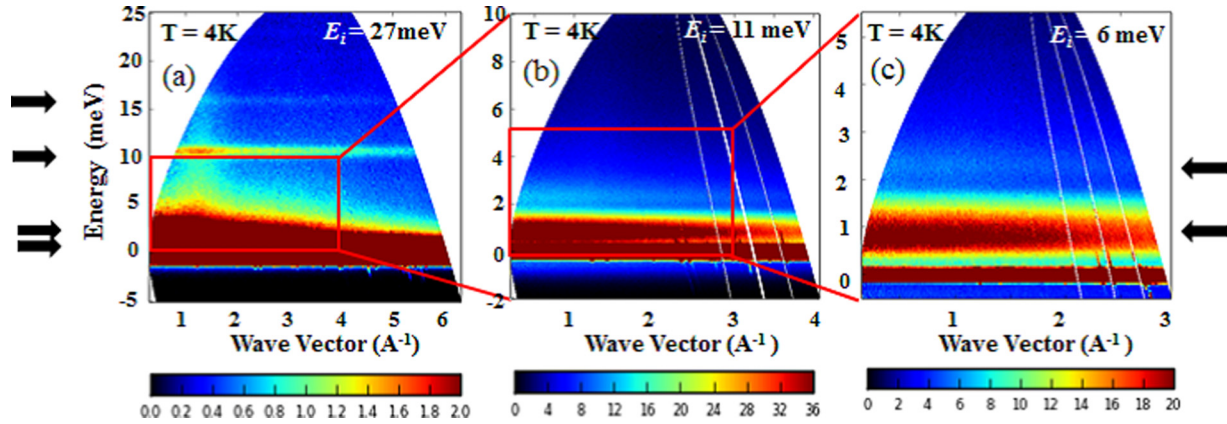
FIG. 2. Map of $I(Q,\omega)$ at 4 K with E_i of (a) 27, (b) 11, and (c) 6 meV. The data have not been corrected using the Bose factor.

with decreasing T. In corner-sharing tetrahedra, all the spins participate in forming one of four different hexagons [see Fig. 4(a), inset], where a network of corner-sharing tetrahedra is shown, for example. The elastic-scattering intensities with $E_i = 6$ and 27 meV as a function of temperature are shown in Fig. 4(c). The difference can be seen, and this is due to the broad range of fluctuations in energy spectra [33].

2. Inelastic-scattering data

For the dispersionless excitations at several discrete energies, which can be seen in Figs. 2 and 3, it is easy to associate them with crystal-field excitations of Ho^{3+} in O_h symmetry, since HBFO involves rare-earth Ho ions. The Hamiltonian of the crystal field of $HoO_6{}^{3-}$ in O_h symmetry is written as

$$\mathscr{H}_{Ho_{CEF}^{3+}} = B_4\left(O_4^0 + 5O_4^4\right) + B_6\left(O_6^0 - 21O_6^4\right),$$

where the O_n^m are angular momentum operators, and B_n are the crystal-field parameters [34,35]. A simplified prediction by Lea, Leak, and Wolf (LLW) [36] is available in cubic

symmetry to obtain the crystal-field parameter for the $\mathscr{H}_{Ho_{CEF}^{3+}}$ Hamiltonian. To obtain the overall possible value of the ratio between B_4 and B_6, we used the reduced form of LLW. Here, $b_4 = B_4F(4) = Wx$, $b_6 = B_6F(6) = W(1 - |x|)$, and $x/(1 - |x|) = F(4)B_4/F(6)B_6 = b_4/b_6$, where $-1 \leqslant |x| \leqslant 1$, W is a scale factor determining the total splitting of the ground-state J multiplet, and F(4) and F(6) are multiplicative factors. Then, we obtain the Ho^{3+} crystal-field excitations in O_h symmetry at 0.9, 2, and 40 meV (and beyond), as shown in Fig. 6 (right), which is almost the same as Ref. [37]. Therefore, the 0.8 and 2.3 meV excitations of HBFO can be ascribed to the CF excitations of Ho^{3+} in octahedral symmetry.

FIG. 4. (a) Elastic scattering profiles ($E_i = 27$ meV) at $T = 4$ and 200 K. The baseline for each profile is displaced. The inset shows the crystal structure of cubic 114 ferrite $HoBaFe_4O_7$. The bold sticks indicate one of the hexagons of Fe spins. The number ratio of Fe^{2+} to Fe^{3+} sites is 3:1. They form corner-sharing tetrahedra. The lattice constants and the bond lengths at 4 and 200 K are shown. (b) Temperature dependences of the elastic diffuse scattering profiles obtained at $E_i = 27$ meV (top) and 6 meV (bottom). (c) Incident energy dependence of the elastic-scattering intensities on $Q = 1.1$ Å^{-1} vs temperature. The Q position is not influenced by Bragg peaks and easily observable temperature change. Throughout this paper, error bars represent standard deviation.
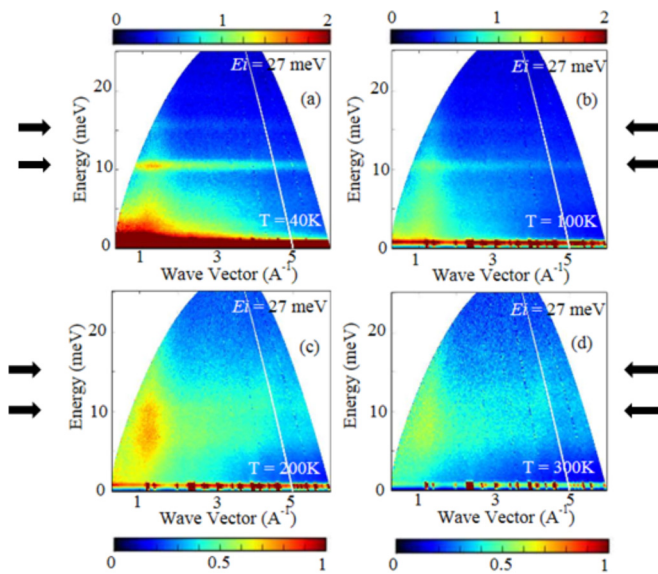

FIG. 3. Map of $\chi''(Q, \omega)$ at T of (a) 40, (b) 100, (c) 200, and (d) 300 K for $E_i = 27$ meV. The data have been corrected using the Bose factor. The data of $T = 4$ K are displayed in Fig. 2(a).
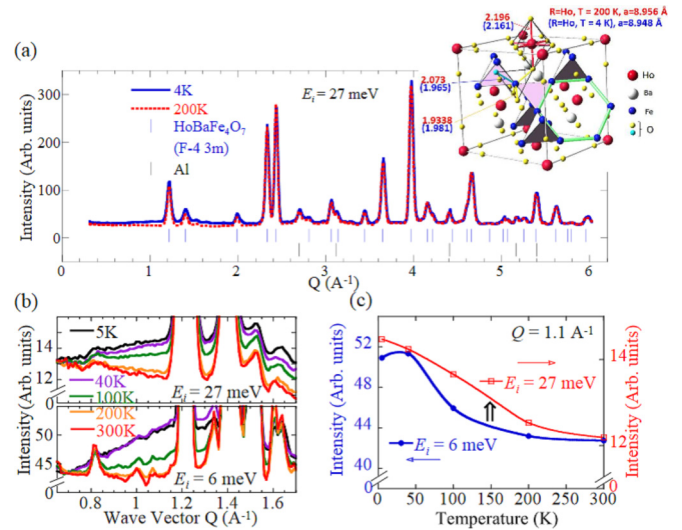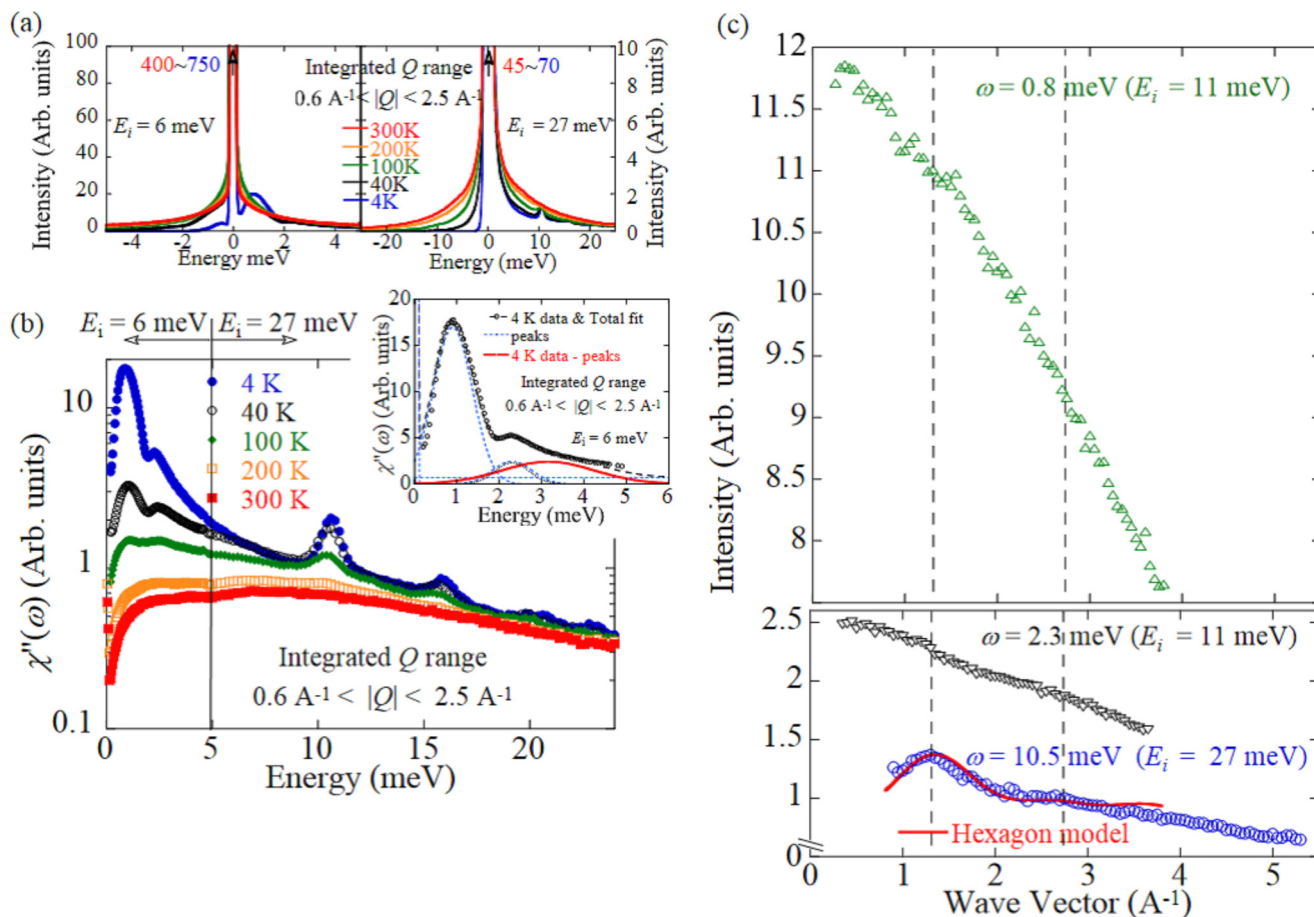
FIG. 5. (a) Energy spectra for several T values with $E_i = 6$ and 27 meV (integrated Q range is $0.6 \leqslant | Q | \leqslant 2.5$ Å^{-1}. (b) Temperature dependences of the dynamical susceptibility $\chi''(\omega)$, which are combined with the $E_i = 6$ and 27 meV data on $\omega = 5$ meV. The inset shows the buried peak (solid line), which was obtained from the data by subtraction of elastic and two CF of Ho^{3+} components (dotted lines). (c) Q profiles at $T = 4$ K for $\omega = 0.8$, 2.3 ($E_i = 11$ meV), and 10.5 meV ($E_i = 27$ meV). The data are obtained from the sliced data (integrated with $\Delta\omega = 0.2$ meV width for $E_i = 11$ meV and $\Delta\omega = 0.4$ meV width for $E_i = 27$ meV) of Fig. 2. The curve of the hexagon model is superimposed on the $\omega = 10.5$ meV data.

The energy spectra at various temperatures with $E_i = 6$ and 27 meV are shown in Fig. 5(a). Here, Q is integrated over $0.6 \leqslant | Q | \leqslant 2.5$ Å^{-1}. Since magnetic scattering signals come only from the dispersionless excitations and the diffuse scattering, we can recognize that the quasielastic scattering originating from the diffuse scattering is less than ~5 meV by the energy spectral data with $E_i = 6$ meV . Figure 5(b) shows the dynamical susceptibility $\chi''(\omega) = I(Q,\omega,T)[1 - \exp(-\hbar\omega/k_B T)]$, and the data are connected on $\omega = 5$ meV with the different incident energies $E_i = 6$ and 27 meV. The peak widths of 0.8 and 2.3 meV excitations are considered to be almost the same. Therefore, we can extract one more peak at 3 meV around the 1.8–5 meV region [see the inset of Fig. 5(b)]. Then, the observed energy levels of the dispersionless excitations are summarized in Fig. 6 (middle). The $\omega = 10.5$ meV excitation shows two peaks at $Q = 1.25$ and 2.7 Å^{-1} [dashed line positions in Fig. 5(c)], which are characterized by a hexagonal spin cluster [see the inset of Fig. 4(a)]. There is a clear difference between the $\omega = 10.5$ meV excitation and the $\omega = 0.8$ and 2.3 meV excitations, which are attributable to the CF excitation of Ho^{3+} in O$_h$ symmetry. The dispersionless
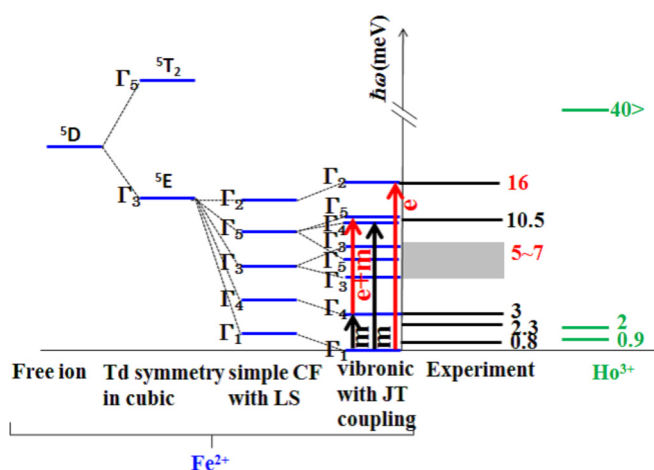

FIG. 6. From left to right: schematic energy levels of estimated Fe^{2+} and actually observed excitation energy levels, and schematic energy scheme of estimated Ho^{3+} CF levels. In the vibronic mode of Fe^{2+} splitting, the transitions are displayed and the selection rule is labeled. The m, e, and $m + e$ labels denote magnetic, electronic, and magnetic+electronic origin, respectively.

excitations at 3, 10.5, 5–7, and 16 meV are not simply attributed to the CF origin of Ho^{3+} in O_h symmetry.

As mentioned in Figs. 2 and 3, the dispersionless excitations can be confirmed clearly at 0.8, 2.3, 10.5, and 16 meV, although that of 5–7 meV looks obscure. With increasing T, all inelastic peak intensities decrease, indicating their magnetic origin. In addition, the static Jahn-Teller distortion is not observed in HBFO, although Fe^{2+} in tetrahedral (T_d) symmetry is a Jahn-Teller active ion, and it normally brings lattice distortion to the system. In this case, we can expect the dynamical Jahn-Teller effect to result in multiplet splitting of the Fe^{2+} magnetic ion state (vibronic mode) [38,39]. Here, Fe^{3+} in T_d symmetry brings only the $^6S_{5/2}$ state, and no contribution is expected to the lattice distortion. The spin Hamiltonian $\mathscr{H}_{Fe^{2+}}$ including orbit-spin coupling is described as

$$\mathscr{H}_{Fe^{2+}} = \mathscr{H}_0 + V_c(T_d) + \lambda LS + \mathscr{H}_{ss} + \mathscr{H}_{dJT},$$
$$\mathscr{H}_{ss} = -\rho[(LS)^2 + (1/2)LS - (1/3)L(L+1)S(S+1)],$$

where $\mathscr{H}_0$ is a free-ion Hamiltonian, $V_c(T_d)$ is the tetrahedral potential, λ is the strength of the spin-orbit interaction, $\mathscr{H}_{ss}$ is the spin-orbit interaction Hamiltonian, ρ is the spin-spin interaction, L is the orbital angular momentum, S is the spin angular momentum, and $\mathscr{H}_{dJT}$ is the Hamiltonian of the dynamical Jahn-Teller interaction, that is, the electron-phonon coupling.

Detailed theoretical treatments can be found elsewhere, and we took some parameters from previous works [40–43] and obtained parameters of the Hamiltonian to reproduce the discrete energy levels: $\lambda = 11.5$ meV, $\rho = 0.12$ meV, and effective orbit-spin splitting energy $\delta = 6(\lambda^2/\Delta + \rho) = 2.34$ meV. Here, Δ is the energy separation between $^5T_2$ and ^5E, taking an approximate value with 620 meV. We also obtained the $E(\Gamma_3)$ state from the transverse branch by the Jahn-Teller coupling energy $\hbar\omega = 1.0$ meV. The results for the energy levels of Fe^{2+} in T_d symmetry are summarized in Fig. 6 (left-middle). The labels m, e, and $e+m$ denote the selection rule of magnetic (m) and electric (e) transitions [38,40–43], and the $e+m$ mode indicates coupling of spin-orbit-lattice degrees of freedom. In fact, the T dependences of the peak intensities at $\omega = 3$ meV (m) and 10.5 meV (m) are different from those of 5–7 meV $(e+m)$ and 16 meV (e), which are in accordance with the selection rules. With regard to the existence of the hexagonal clusters mentioned above, we tried to explain the energy level scheme using an isolated hexagonal spin ring model of Fe^{2+} as in Refs. [44,45] because some discrete dispersionless excitations have been successfully described by the isolated spin ring model [12]. However, the isolated spin ring model could not reproduce the energy scheme of the present system. Although there are some explanations for the similar discrete energy levels by electromagnetic splitting [46,47], local resonance inelastic scattering [48], etc., we think that the treatment of a vibronic state by the dynamical Jahn-Teller effect has something to do with the isolated spin ring model treatment, but it has not been solved yet.

C. Scaling rule

The scaling rule of HBFO has been studied to compare that of YBFO [17]. By profiling from previous works [49–51], the
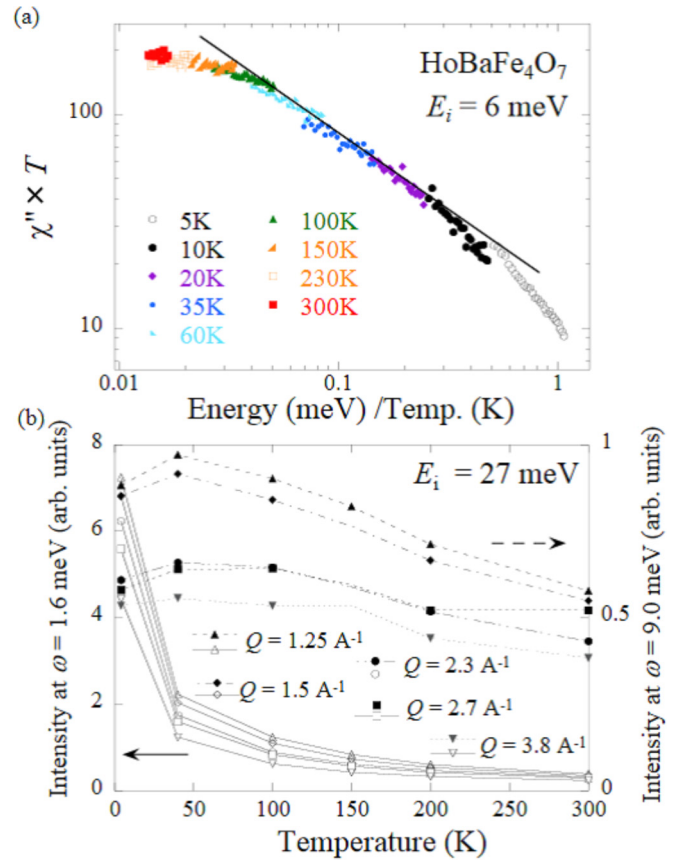

FIG. 7. (a) χT^α ($\alpha = 1$) vs ω/T plots on log-log scales. The solid line is a guide for the eye. (b) Temperature dependences of the inelastic scattering intensity on $\omega = 1.6$ and 9.0 meV at several Q positions. The data are obtained from Figs. 2 and 3 (integrated with $\Delta Q = 0.2 \text{ Å}^{-1}$ widths).

$\chi''(\omega)T^\alpha$ versus ω/T scaling plot is generated in Fig. 7(a). Here, $\chi''a(\omega)$ is used from Fig. 5(b) and the integration does not affect $\chi''(\omega)$, as mentioned in Figs. 5(a) and 5(b). We found $\alpha = 1$ in the T range between about 20 and 150 K. This scaling rule indicates that the spin dynamics of HBFO can be treated by a model of typical spin glass, whereas the spin dynamics of YBFO suggested a quantum critical phenomenon with $\alpha = 1/3$ [17]. However, no spin-glass-like behavior is observed, at least in the magnetic susceptibility of HFBO. Figure 7(b) shows the temperature dependences of the scattering intensities at $\omega = 1.6$ and 9 meV on several Q positions. To avoid any disturbance of dispersionless excitations, we selected the $\omega = 1.6$ and 9 meV positions. The $Q \sim 1.25$ and 2.7 Å^{-1} points were chosen as positions of the dominating diffuse scattering, while the other Q points were chosen as positions that are free from diffuse scattering. The tail of the diffuse scattering, namely quasielastic scattering, is decreasing as the temperature increases. On the other hand, the intensity at $\omega = 9$ meV as a representative position of 5–10 meV becomes maximum around 40 K. Since all intensities are decreasing as temperature and Q increase, these physical features are attributable to the magnetic origin. At first glance, it appears that there are two components, but this can be understood simply as one-component behavior with a

gradually change from quasielastic scattering (of the magnetic diffuse scattering) to inelastic scattering around 40 K. As the temperature increases, thermal fluctuation becomes dominant and magnetic correlations become obscure. The behavior is a typical feature of spin glass, and we can see similar behavior in another frustrated magnet [52].

In $R =$ Ho, the spin fluctuation of Fe ions seems to be weaker than that of $R =$ Y, and it is considered to be suppressed by the existence of the Ho ion. This may be due to an effect of Ho ions on Fe spins, although we have not considered the interaction of energy modes between Ho^{3+} CF and Fe^{2+} of the dynamical Jahn-Teller effect. We suppose that the time scale of the Fe-ion dynamics becomes close to that of the lattice dynamics. Then the interaction among them emerges, and the vibronic modes appear. The dynamic Jahn-Teller effect is achieved via the synergistic effect of the dynamics brought about by the frustration effect, so the appearance of a vibronic mode would be a feature of the frustration effect. It would be necessary to investigate the influence of the moment size of R by using different R ions.

IV. CONCLUSION

The inelastic neutron-scattering experiment has been carried out on $HoBaFe_4O_7$ with a 3D network of corner-sharing tetrahedra of Fe atoms. In contrast to $YBaFe_4O_{7-\delta}$, the HFBO has dispersionless excitations at several discrete energies. Some energy levels cannot be attributed to the crystal field excitations of Ho^{3+} in octahedral symmetry. Instead, some levels can be explained by considering vibronic state of the Fe^{2+} dynamical Jahn-Teller effect with orbit-spin coupling, indicating that spin-orbital-lattice degrees of freedom are coupled to each other. The difference of the R ion affects the dynamics of this frustrated system, $RBaFe_4O_7$, resulting in rich varieties of characteristic excitation such as the strong spin fluctuations over a wide energy range at a characteristic wave vector, or the dynamical interaction among spin-orbital-lattice degrees of freedom of isolated spin clusters.

[1] J. E. Greedan, J. Alloys Compd. **408-412**, 444 (2006).

[2] J. S. Gardner, M. J. P. Gingras, and J. E. Greedan, Rev. Mod. Phys. **82**, 53 (2010).

[3] S.-H. Lee, H. Takagi, D. Louca, M. Matsuda, S. Ji, H. Ueda, Y. Ueda, T. Katsufuji, J.-H. Chung, S. Park, S.-W. Cheong, and C. Broholm, J. Phys. Soc. Jpn. **79**, 011004 (2010).

[4] R. Ballou, E. Lelièvre-Berna, and B. Fåk, Phys. Rev. Lett. **76**, 2125 (1996).

[5] K. Kamazawa, Y. Tsunoda, K. Odaka, and K. Kohn, J. Phys. Chem. Solids **60**, 1261 (1999).

[6] S.-H. Lee, C. Broholm, W. Ratcliff, G. Gasparovic, Q. Huang, T. H. Kim, and S.-W. Cheong, Nature (London) **418**, 856 (2002).

[7] S. T. Bramwell, M. J. Harris, B. C. den Hertog, M. J. P. Gingras, J. S. Gardner, D. F. McMorrow, A. R. Wildes, A. L. Cornelius, J. D. M. Champion, R. G. Melko, and T. Fennell, Phys. Rev. Lett. **87**, 047205 (2010).

[8] Y. Yasui, M. Kanada, M. Ito, H. Harashina, M. Sato, H. Okumura, K. Kakurai, and H. Kadowaki, J. Phys. Soc. Jpn. **71**, 599 (2002).

[9] J. S. Gardner, B. D. Gaulin, A. J. Berlinsky, P. Waldron, S. R. Dunsiger, N. P. Raju, and J. E. Greedan, Phys. Rev. B **64**, 224416 (2001).

[10] J. A. M. Paddison, H. Jacobsen, O. A. Petrenko, M. T. Fernández-Díaz, P. P. Deen, and A. L. Goodwin, Science **350**, 179 (2015).

[11] J. A. M. Paddison and A. L. Goodwin, Phys. Rev. Lett. **108**, 017204 (2012).

[12] K. Tomiyasu, T. Yokobori, Y. Kousaka, R. I. Bewley, T. Guidi, T. Watanabe, J. Akimitsu, and K. Yamada, Phys. Rev. Lett. **110**, 077205 (2013).

[13] H. J. Silverstein, K. Fritsch, F. Flicker, A. M. Hallas, J. S. Gardner, Y. Qiu, G. Ehlers, A. T. Savici, Z. Yamani, K. A. Ross, B. D. Gaulin, M. J. P. Gingras, J. A. M. Paddison, K. Foyevtsova, R. Valenti, F. Hawthorne, C. R. Wiebe, and H. D. Zhou, Phys. Rev. B **89**, 054433 (2014).

[14] D. Reig-i-Plessis, D. Casavant, V. O. Garlea, A. A. Aczel, M. Feygenson, J. Neuefeind, H. D. Zhou, S. E. Nagler, and G. J. MacDougall, Phys. Rev. B **93**, 014437 (2016).

[15] S. Petit, S. Guitteny, J. Robert, P. Bonville, C. Decorse, J. Ollivier, H. Mutka, and I. Mirebeau, EPJ Web Conf. **83**, 03012 (2015).

[16] A. P. Ramirez, G. P. Espinosa, and A. S. Cooper, Phys. Rev. Lett. **64**, 2070 (1990).

[17] K. Kamazawa, M. Ishikado, S. Ohira-Kawamura, K. Kakurai, K. Nakajima, Y. Kawakita, K. Yamada, M. Arai, and M. Sato, J. Phys. Soc. Jpn. **84**, 104711 (2015).

[18] This information was obtained using another spectrometer, SIKI (BL01), at MLF of J-PARC.

[19] M. Shiga, H. Wada, Y. Nakamura, J. Deporters, B. Ouladdiaf, and K. R. A. Ziebeck, J. Phys. Soc. Jpn. **57**, 3141 (1988).

[20] B. D. Rainford, S. Dakin, and R. Cywinski, J. Magn. Magn. Mater. **104-107**, 1257 (1992).

[21] J. R. Stewart, G. Ehlers, H. Mutka, P. Fouquet, C. Payen, and R. Lortz, Phys. Rev. B **83**, 024405 (2011).

[22] K. Kamazawa and T. Moyoshi (unpublished).

[23] V. Pralong, V. Caignaert, A. Maignan, and B. Raveau, J. Mater. Chem. **19**, 8335 (2009).

[24] V. Caignaert, A. M. Abakumov, D. Pelloquin, V. Pralong, A. Maignan, G. Van Tendeloo, and B. Raveau, Chem. Mater. **21**, 1116 (2009).

[25] V. Duffort, V. Caignaert, V. Pralong, N. Barrier, B. Raveau, M. Avdeev, H. Zheng, and J. F. Mitchell, J. Solid State Chem. **191**, 225 (2012).

[26] V. Duffort, T. Sarkar, V. Caignaert, V. Pralong, B. Raveau, M. Avdeev, A. Cervellino, J. C. Waerenborgh, and E. V. Tsipis, J. Solid State Chem. **205**, 225 (2013).

[27] E. J. W. Verwey and P. W. Haayman, Physica **8**, 979 (1941).

[28] E. J. W. Verwey, P. W. Hayman, and C. W. Romeijn, J. Chem. Phys. **15**, 181 (1947).

[29] F. Walz, J. Phys.: Condens. Matter **14**, R285 (2002).

[30] K. Nakajima, S. Ohira-Kawamura, T. Kikuchi, M. Nakamura, R. Kajimoto, Y. Inamura, N. Takahashi, K. Aizawa, K. Suzuya, K. Shibata, T. Nakatani, K. Soyama, R. Maruyama, H. Tanaka, W. Kambara, T. Iwahashi, Y. Itoh, T. Osakabe, S. Wakimoto, K. Kakurai, F. Maekawa, M. Harada, K. Oikawa, R. E. Lechner, F. Mezei, and M. Arai, J. Phys. Soc. Jpn. **80**, SB028 (2011).

[31] Y. Inamura, K. Nakajima, R. Kajimoto, T. Nakatani, M. Arai, T. Otomo, J. Suzuki, J. Y. So, and J. G. Park in *Proceeding of the 19th Meeting of the International Collaboration on advanced Neutron*, Paul Scherrer Institut, PSI-proceedings 10-01 (2010); Y. Inamura, T. Nakatani, J. Suzuki, and T. Otomo, J. Phys. Soc. Jpn. **82**, SA031 (2013).

[32] G. Shirane, D. E. Cox, and S. J. Pickart, J. Appl. Phys. **35**, 954 (1964).

[33] A. P. Murani and A. Heidemann, Phys. Rev. Lett. **41**, 1402 (1978).

[34] M. H. Hutchings, Solid State Phys. **16**, 1381 (1963).

[35] R. J. Elliott and K. W. H. Stevens, Proc. R. Soc. London, Ser. A **218**, 553 (1953).

[36] K. R. Lea, M. J. M. Leask, and W. P. Wolf, J. Phys. Chem. Solids **23**, 1381 (1962).

[37] S. Calder, X. Ke, F. Bert, A. Amato, C. Baines, C. Carboni, R. J. Cava, A. Daoud-Aladine, P. Deen, T. Fennell, A. D. Hillier, H. Karunadasa, J. W. Taylor, P. Mendels, P. Schiffer, and S. T. Bramwell, Phys. Rev. B **81**, 064425 (2010).

[38] A. Krimmel, M. Mücksch, V. Tsurkan, M. M. Koza, H. Mutka, and A. Loidl, Phys. Rev. Lett. **94**, 237402 (2005).

[39] S. Nakatsuji, K. Kuga, K. Kimura, R. Satake, N. Katayama, E. Nishibori, H. Sawa, R. Ishii, M. Hagiwara, F. Bridges, T. U. Ito, W. Higemoto, Y. Karaki, M. Halim, A. A. Nugroho, J. A. Rodriguez-Rivera, M. A. Green, and C. Broholm, Science **336**, 559 (2012).

[40] J. T. Vallin, Phys. Rev. B **2**, 2390 (1970).

[41] C. Testelin, C. Rigaux, A. Mauger, A. Mycielski, and C. Julien, Phys. Rev. B **46**, 2183 (1992).

[42] D. Colignon, E. Kartheuser, S. Rodriguez, and M. Villeret, Phys. Rev. B **51**, 4849 (1995).

[43] D. Colignon, E. Kartheuser, and M. Villeret, J. Phys.: Condens. Matter **12**, 2691 (2000).

[44] O. Waldmann, Phys. Rev. B **65**, 024424 (2001).

[45] M. L. Baker, T. Guidi, S. Carretta, J. Ollivier, H. Mutka, H. U. Güdel, G. A. Timco, E. J. L. McInnes, G. Amoretti, R. E. P. Winpenny, and P. Santini, Nat. Phys. **8**, 906 (2012).

[46] S. Ligenza and H. Ptasiewicz-Bak, Phys. Status Solidi B **90**, 319 (1978).

[47] S. Ligenza, Phys. Status Solidi B **75**, 315 (1976).

[48] S.-H. Lee, C. Broholm, T. H. Kim, W. Ratcliff II, and S.-W. Cheong, Phys. Rev. Lett. **84**, 3718 (2000).

[49] B. Fåk, F. C. Coomer, A. Harrison, D. Visser, and M. E. Zhitomirsky, Europhys. Lett. **81**, 17006 (2008).

[50] M. A. de Vries, J. R. Stewart, P. P. Deen, J. O. Piatek, G. J. Nilsen, H. M. Rønnow, and A. Harrison, Phys. Rev. Lett. **103**, 237201 (2009).

[51] J. S. Helton, K. Matan, M. P. Shores, E. A. Nytko, B. M. Bartlett, Y. Qiu, D. G. Nocera, and Y. S. Lee, Phys. Rev. Lett. **104**, 147201 (2010).

[52] K. Kamazawa, H. Nozaki, M. Harada, K. Mukai, Y. Ikedo, K. Iida, T. J. Sato, Y. Qiu, M. Tyagi, and J. Sugiyama, Phys. Rev. B **83**, 094401 (2011).